ACS APPLIED MATERIALS & INTERFACES

www.acsami.org

Research Article

Deciphering the Structure–Property Relationship of Na–Mn–Co–Mg–O as a Novel High-Capacity Layered–Tunnel Hybrid Cathode and Its Application in Sodium-Ion Capacitors

Hyun-Jae Kim,[‡] Hari Vignesh Ramasamy,[‡] Gang-Hyeon Jeong, Vanchiappan Aravindan, and Yun-Sung Lee*

Cite This: *ACS Appl. Mater. Interfaces* 2020, 12, 10268–10279

Read Online

ACCESS | Metrics & More | Article Recommendations | Supporting Information

ABSTRACT: Developing novel cathode materials with a high energy density and long cycling stability is necessary for Na-ion batteries and Na-ion hybrid capacitors (NICs). Despite their high energy density, structural flexibility, and ease of synthesis, P-type Na layered oxides cannot be utilized in energy-storage applications owing to their severe capacity fading. In this regard, we report a novel composite layered–tunnel $Na_{0.5}Mn_{0.5}Co_{0.48}Mg_{0.02}O_2$ cathode whose binary structure was confirmed via scanning electron microscopy and high-resolution transmission electron microscopy. Combination of the two-dimensional (2D) layered oxides with the three-dimensional tunnel structure, as well as the presence of Mg^{2+} ions, resulted in a high capacity of 145 mAh g^{-1} at a current density of 85 mA g^{-1}, along with a high stability and rate capability. An NIC was fabricated with composite layered-tunnel structure as a battery-type electrode and commercial activated carbon as a counter electrode. The NIC exhibited a maximum energy density of 35 Wh kg^{-1} and good stability retaining 72% of its initial energy density after 3000 cycles. This integrated approach provides a new method for designing high-energy and high-power cathodes for NICs and NIBs.

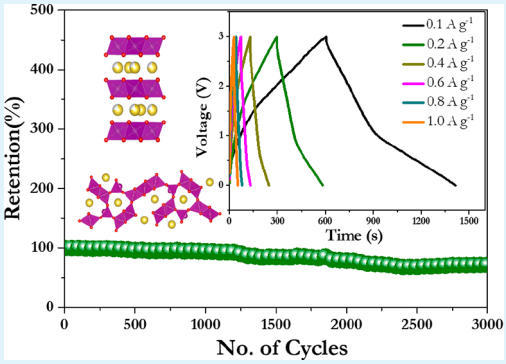

KEYWORDS: *layered structure, tunnel structure, cathode, biphase, sodium-ion capacitor*

INTRODUCTION

The global energy crisis has driven the search for advanced energy-storage devices that can efficiently store energy from sustainable sources like solar and wind. Electrochemical energy-storage devices with high energy and power densities are important for many applications, such as electric vehicles and hybrid electric vehicles.[1] Currently, Li-ion batteries are dominant energy-storage devices owing to their high energy density and lightweight.[2] However, these batteries are expensive because of the limited availability of Li resources, which are situated in geographically sensitive areas. This has encouraged the scientific community to focus on sustainable Na-based energy-storage devices.[3] Owing to the abundance and low cost of Na, Na-ion batteries (NIBs) are considered to be excellent storage devices for grid storage applications and can be one of the leading next-generation energy-storage devices promoting sustainable global economic growth.[4] The working principle of NIBs is similar to that of LIBs in that the cations/anions migrate across the separator toward the electrodes to realize voltage-driven electrochemical reactions.[5] Graphite is a commercially successful anode for LIBs, but its performance has failed to translate to NIBs, owing to the large size of Na^+ ions. Nonetheless, several high-capacity anode materials with good performance have been reported.[6] However, the problem lies in finding a suitable electrode capable of reversibly intercalating Na ions with high stability under long-term cycling.

Electrochemical capacitors are important energy-storage devices that cater to high-power applications such as grid/voltage stabilization, regenerative braking for automobiles, and uninterruptible power supplies. These capacitors store charges via reversible ion adsorption on the surface of the electrode, resulting in high power density and cycling stability. However, the limited energy density (one order of magnitude lower than that of LIBs) is a serious drawback compared with other charge-storage devices.[7] Consequently, efforts are increasingly directed toward the fabrication of a novel device with high-energy and high-power characteristics. The Li-ion capacitor (LIC) was introduced by Amatucci et al. in 2001 and later attracted considerable attention from the scientific community.[8] The LIC is composed of a battery-type electrode and a capacitor-type electrode in an aprotic organic medium with

Received: October 25, 2019
Accepted: February 10, 2020
Published: February 10, 2020

https://dx.doi.org/10.1021/acsami.9b19288
ACS Appl. Mater. Interfaces 2020, 12, 10268–10279

two different charge-storage mechanisms in a single framework. JM Energy and JSR Micro have commercialized the graphite//activated carbon (AC)-based LIC; however, the limited supply of Li justifies its replacement with Na, which is more abundant.[9] Several Na-ion-based battery-type electrodes have been reported for NIC applications. The choice of a suitable electrode material is very important for realizing the high energy density of the hybrid system, for example, Na–TNT,[10] UTH–CNs,[11] N-doped carbon,[12] m-Nb_2O_5–C,[13] T–Nb_2O_5,[14] $Na_{0.44}MnO_2$,[15] $Na_3(VO)_2(PO_4)_2F$,[16] Na_2CoSiO_4,[17] CNT–Nb_2O_5,[18] V_2O_5–CNT,[19] $NiCo_2O_4$,[20] Nb_2O_5–NS,[21] and TiO_2–B nanorods,[22] 2D MOF-based electrodes,[23] and TiS_2.[24] In our previous study, we utilized a bottom-up approach for the synthesis of battery-type intercalation hosts for NIC applications, and the results were promising.[25−28] Hence, developing a novel battery-type intercalation host as an electrode with high capacity, excellent rate performance, and long-term cycling stability is necessary for the fabrication of high-energy NICs. AC is the preferred and unanimous choice for the electric double-layer capacitor (EDLC) component owing to its high electrical conductivity, excellent chemical stability under different pH conditions, large specific surface area with tailored porosity, low cost, and environmental friendliness.[29]

Among the many reported battery-type electrodes, layered oxides comprising stacked $(MO_2)_n$ sheets with MO_6 edge-sharing octahedral units have a high capacity and good feasibility.[30−32] The Na ions between the layers can have prismatic or octahedral coordination and are denoted as P-type or O-type, respectively. They can be further classified as P2, P3, or O3.[33] Compared with the O3-type structure, which undergoes a complex phase change at high voltages, the P2 structure is more stable in a wider voltage window. This is due to the wider diffusion channel with a lower energy barrier against migration. In addition, P2-type oxides provide more flexibility in design, allowing two or more transition-metal ions in the structure for better performance.[34] Layered $NaMnO_2$ was first reported by Parant et al.,[35] and since then, Mn-based cathodes have been preferred as safe and sustainable cathodes for efficient Na-ion intercalation/deintercalation.[36] Despite their good performance, these layered oxides have not yet been utilized as a cathode for NICs owing to their inferior rate performance and stability. Jahn–Teller distortion is generally observed for six-coordinate Mn(III) consisting of a high-spin ($t_{2g}^3e_g^1$) electronic structure, which is disadvantageous for its electrochemical performance.[37] In addition, the high-voltage P2–O2 phase transition accompanied by a two-dimensional (2D) ion migration pathway is a prime concern.[38] Several methods, such as doping and surface modification, are employed to improve the stability by suppressing the phase transition and Mn dissolution.[39]

A tunnel-type Na_xMnO_2 structure is formed when the composition of Na is between 0.22 and 0.44. This is an attractive candidate for NIC applications owing to its unique three-dimensional (3D) structure composed of MnO_5 pyramids and MnO_6 octahedra arranged in a large S-shaped tunnel and a smaller pentagon tunnel with maximum stress tolerance during charge–discharge. It has a theoretical capacity of 121 mAh g^{-1}, resulting from the reversible Na-ion insertion/extraction along the *c* axis accompanied by the abundant vacancies of the large S tunnel.[40,41] Both layered and tunnel structures have drawbacks for practical applications. Many pioneering studies have been performed on Na-ion batteries in which two or more structures were combined to overcome these drawbacks.[42−53]

In this regard, we designed $Na_{0.5}Mn_{0.5}Co_{0.48}Mg_{0.02}O_2$ as a novel high-capacity layered–tunnel hybrid cathode material with high electrochemical performance via a facile sol–gel synthesis method and investigated it as a battery-type electrode for an NIC. Prior to the assembly, the structure and morphology of the hybrid structure were thoroughly examined using transmission electron microscopy (TEM), and the physiochemical properties were evaluated. The half-cell performance of $Na_{0.5}Mn_{0.5}Co_{0.48}Mg_{0.02}O_2$ and AC was investigated to balance their masses in the NIC. This novel NIC exhibited a high energy density of 34 Wh kg^{-1} with excellent cyclic stability, retaining >72% of its initial energy density after 3000 cycles at 1 A g^{-1}. The superior Na-storage capability of this novel hybrid cathode provides possibilities for investigating new insertion hosts for high-performance NIC configurations.

EXPERIMENTAL SECTION

Synthesis. We used a facile citric acid-assisted sol–gel route for the synthesis of P2 $Na_{0.5}Mn_{0.5}Co_{0.5}O_2$ and P2 $Na_{0.5}Mn_{0.5}Co_{0.48}Mg_{0.02}O_2$. In a typical process, a stoichiometric amount of sodium acetate (CH_3COONa, Sigma-Aldrich) with 5% extra to compensate for the Na loss due to higher temperature calcination, manganese acetate tetrahydrate ($Mn(CH_3COO)_2{\cdot}4H_2O$, Sigma-Aldrich), magnesium acetate hexahydrate ($Mg(CH_3COO)_2{\cdot}4H_2O$, Sigma-Aldrich), and cobalt acetate tetrahydrate ($Co(CH_3COO)_2{\cdot}4H_2O$, Sigma-Aldrich) were dissolved separately in deionized water with stirring for 30 min until complete dissolution of the respective metal precursors was achieved. Later, the mixed precursor solution was added dropwise to an aqueous solution of citric acid (80 wt %). The final solution was stirred at 80 °C until gel formation. The gel precursor was kept at 120 °C overnight to obtain the precursor. The dried powder was subjected to heat treatment at 500 °C to decompose the acetate and water moieties. Then the sample was ground, pelletized, and heated at 900 °C for 15 h to obtain the final product.

Characterization. X-ray diffraction (XRD; Cu Kα radiation, Rint 1000, Rigaku, Japan) patterns of the samples were obtained. Rietveld analysis was performed using Fullprof software to investigate the structural change after metal ion doping. The elemental compositions of the samples were analyzed using inductively coupled plasma (ICP) atomic energy spectroscopy (PerkinElmer, OPTIMA 8300, USA). The valence states of the elements were identified using X-ray photoelectron spectroscopy (XPS, MultiLab 2000, UK). The morphology and microstructure of the samples were analyzed using field-emission scanning electron microscopy (SEM, S-4700, Hitachi, Japan), selected-area electron diffraction (SAED), energy-dispersive X-ray spectroscopy (EDS), and high-resolution TEM (HR-TEM; JEM-2000, EX-II, JEOL, Japan).

Electrochemical Studies. The electrochemical performance of all of the samples was evaluated using CR2032 coin-cell assemblies in an Ar-filled glovebox, where the O_2 and H_2O concentrations were maintained well below 1 ppm. The synthesized material was used as the cathode, and Na metal was used as the anode. Whatman glass fiber filter paper was used as a separator, and 1 M $NaClO_4$ in propylene carbonate with 5 wt % fluoroethylene carbonate was used as an electrolyte. The total composition of the electrode was as follows: 80% active material (20 mg), 10% conductive additive (Ketjenblack), and 10% binder (Teflonized acetylene black, TAB-2). The obtained slurry was pressed on a stainless-steel mesh current collector using a hydraulic press and dried in a vacuum oven at 160 °C for 4 h before cell fabrication. The electrochemical properties of the material were evaluated via cyclic voltammetry (CV) using an electrochemical workstation (Biologic, SP-150, France) at different scan rates ranging from 0.1 to 0.5 mV s^{-1}. Galvanostatic charge–

https://dx.doi.org/10.1021/acsami.9b19288
ACS Appl. Mater. Interfaces 2020, 12, 10268−10279

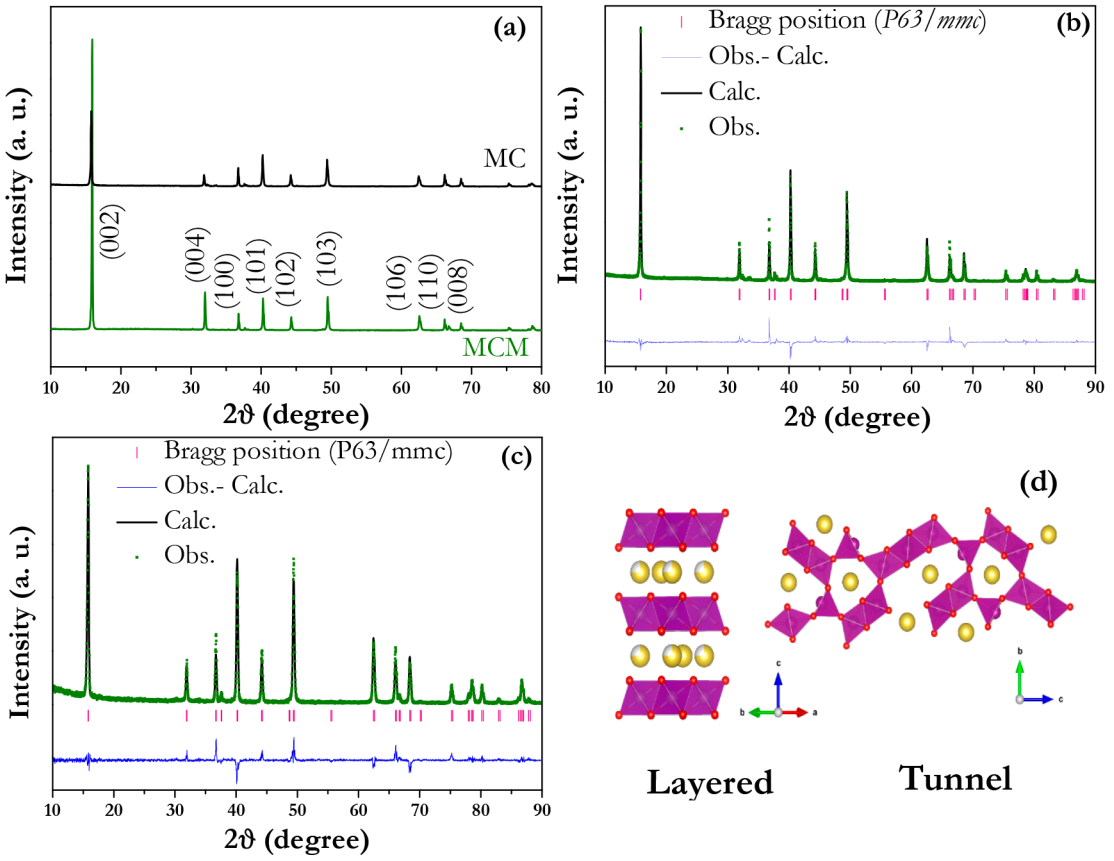

Figure 1. (a) XRD patterns of the MC and MCM samples. Rietveld refined peaks of (b) MC and (c) MCM. (d) Schematic of the P2-layered and tunnel structure.

discharge tests were conducted using a battery cycler (WBCS 3000, WonATech) with different cutoff potentials. The rate performance was evaluated at different current rates (0.5, 1.0, 2.0, 4.0, and 10 C) with 10 cycles each. Electrochemical impedance spectroscopy (EIS) was performed on the cells before and after cycling. Here, the frequency was varied from 100 kHz to 10 mHz with an alternating-current amplitude of 10 mV. All of the measurements were performed at ambient temperature (25 °C).

RESULTS AND DISCUSSION

$Na_{0.5}Mn_{0.5}Co_{0.5}O_2$ and $Na_{0.5}Mn_{0.5}Co_{0.48}Mg_{0.02}O_2$ compounds were synthesized using a sol−gel method, and their actual compositions were determined using ICP analysis. The values of Na:Mn:Co:Mg are 0.496:0.51:0.499:0 for MC and 0.495:0.505:0.497:0.021 for MCM samples. These values match well with the actual composition. The crystal structures of both samples were analyzed using XRD, and all of the diffraction peaks well matched the hexagonal lattice corresponding to the P2 structure (similar to P2−$Na_{2/3}CoO_2$) (Figure 1a).[54] Partial substitution of Mg for Co was clearly indicated by the deviation in the lattice-parameter values, i.e., *a* and *b* increased from 2.820 to 2.825 Å, whereas *c* decreased from 11.213 to 11.207 Å. This decrease in *c* was supported by the shift in the XRD peak (002) toward a larger angle. Despite this decrease in the *c* axis, Mg doping tended to reduce the *d* spacing, as reported.[55] The Mg^{2+} ions also partially occupied the Na^+ site, which is the reason for the shift of the (002) plane and formation of the tunnel structure. This is further confirmed by the ICP values reported above. We carried out the Rietveld refinement (Figure 1b and 1c) for XRD, and the

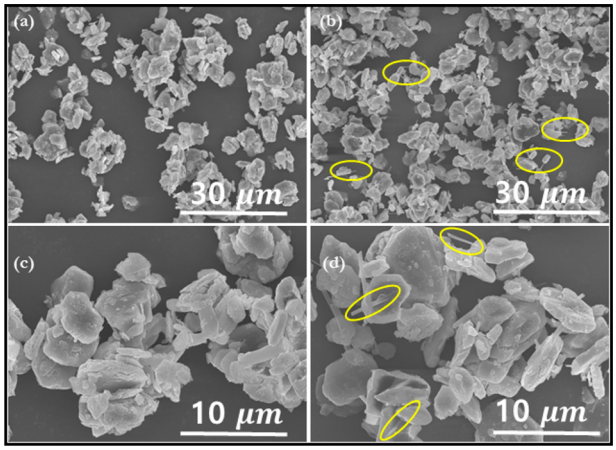

Figure 2. SEM images of the (a, c) MC and (b, d) MCM samples. Yellow circles denote the tunnel structure.

calculated peaks well match with the observed ones. R_p values for MC and MCM are 11.9% and 9.38%, respectively. The atomic occupancies of the samples are provided in Tables S1 and S2. From the above studies, it is clear that the presence of the tunnel structure is not detected in XRD analyses. The crystal structures of P2-layered and tunnel structures are provided in Figure 1d. To understand the structure−property relationship of these layered oxides we doped MC with different concentrations of Mg, and the XRD patterns are given in Figure S1. The increasing concentration of Mg ions does not produce additional peaks of tunnel structure in the XRD

https://dx.doi.org/10.1021/acsami.9b19288
ACS Appl. Mater. Interfaces 2020, 12, 10268−10279

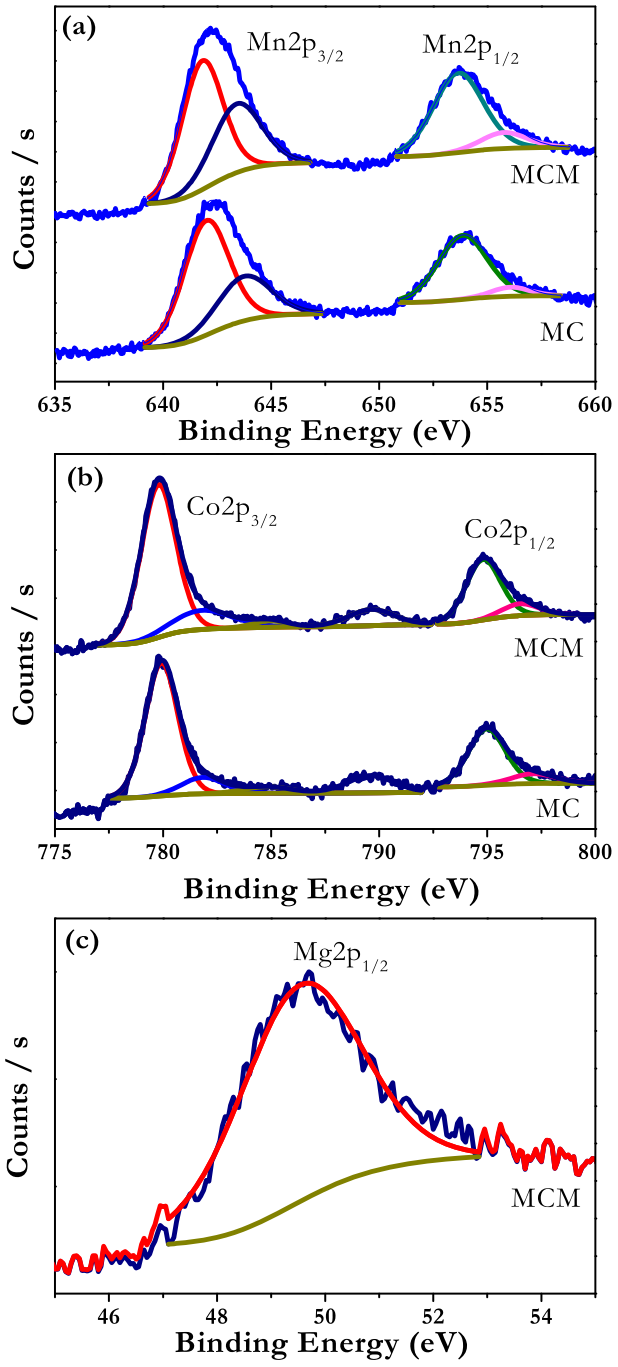

Figure 3. Deconvoluted X-ray photoelectron spectra of (a) Mn, (b) Co, and (c) Mg for the MC and MCM samples.

pattern. SEM images revealed the morphologies of the sample at low and high magnifications. Figure 2a shows a low-magnification image of the $Na_{0.5}Mn_{0.5}Co_{0.5}O_2$ (MC) sample, which exhibited uniformly shaped hexagonal microparticles with an average size of 5−10 μm. Figure 2b indicates that similar hexagonal microparticles were present even after the doping with Mg ions, and the magnified images in Figure 2c and 2d shed further light on the morphology. Needle-like nanoparticles with a size of ≤200 nm were sparsely distributed in the Mg-doped sample in addition to the hexagonal particles (Figure 2d). The MC sample did not have this type of needle-like structure. The needle-like structures are highlighted by a yellow circle and are sparsely distributed in MCM only. The oxidation states of the individual elements were confirmed using XPS (Figure 3a and 3c). The X-ray photoelectron spectrum of Mn was deconvoluted into four peaks at binding energies of 642, 653.86, 643.75, and 656.06 eV. The former two peaks at lower binding energies were associated with Mn^{3+}, and the latter two corresponded to Mn^{4+}.[56] The two main Co peaks were deconvoluted into four peaks at 779.93, 794.97, 781.85, and 797.15 eV. The former two peaks correspond to a low valence state of 3+, and the other two correspond to 4+.[56] Similar peak positions were observed even after doping with a small amount of Mg ions, indicating that the Mg^{2+} ion substitution was successful. In addition to these peaks, the $Na_{0.5}Mn_{0.5}Co_{0.48}Mg_{0.02}O_2$ (MCM) sample exhibited a peak at 49.52 eV corresponding to Mg^{2+}, which was not active in the electrochemical reaction.[57]

A more detailed structural analysis of the MC sample was performed using TEM. Figure 4a shows a single particle of MC with a hexagonal shape, representing the P2 structure with an average particle size of 5 μm. The corresponding selected area electron diffraction (SAED) pattern along the (001) direction exhibits uniform bright spots in the hexagonal pattern, indicating the phase purity and high crystallinity of the sample (Figure 4b). In more detail, the coexistence of the layered and tunnel structure is magnified and provided in Figure 4c and 4d. Figure 4e shows TEM images of MCM needle-shaped particles with a particle size of approximately 200 nm. Compared with the P2-type hexagonal particles, the needle structures were smaller and more sparsely distributed. The SAED pattern shown in Figure 4f provides characteristic spot patterns of the tunnel structure with an orthorhombic lattice (space group $Pmc2_1$) along the 010 plane.[52] The HR-TEM images of the tunnel structure with lattice fringes corresponding to the 010 plane are provided in Figure 4g. Furthur, these layered and tunnel structures are also intergrown as given in Figure 4h, and their SAED pattern and HRTEM images are provided in Figure 4i and 4j. The EDS elemental-mapping results in Figure 4k confirm the uniform distribution of all of the elements in the P2 structure. Figure 4l shows the uniform distribution of elements in the needle structure. The aforementioned SEM and TEM observations clearly indicate that the layered−tunnel hybrid $Na_{0.5}Mn_{0.5}Co_{0.48}Mg_{0.02}O_2$ was a composite cathode with separate layered−tunnel structures resulting from the large variations in the crystal structures. In addition, there were a few single particles in which the layered and tunnel structures were intergrown owing to the compatible close-packed O arrays along some particular axes in both structures. At the initial stage of calcination, the layered oxides were formed from the precursors using available Na. At the final stage of calcination, the insufficient Na resulted in the formation of the tunnel structure.[48]

The electrochemical performance of $Na_{0.5}Mn_{0.5}Co_{0.5}O_2$ and $Na_{0.5}Mn_{0.5}Co_{0.48}Mg_{0.02}O_2$ was evaluated using a half-cell configuration against Na metal via three different analytical techniques.

CV is a powerful method for investigating the redox behavior of different transition metals. The different transition-metal environments and the electrostatic repulsion between the Na cations caused Na^+/vacancy ordering, yielding broad redox peaks within the voltage range of 1.5−4.3 V at a scan rate of 0.5 mV s^{-1} (Figure 5a).[58] In the case of the pristine material, two prominent redox processes occurred: $Mn^{3+/4+}$ coupling in a low-voltage range (~2.0 V vs Na) and the contribution of $Co^{3+/4+}$ in a higher voltage region (>3.5 V vs

https://dx.doi.org/10.1021/acsami.9b19288
ACS Appl. Mater. Interfaces 2020, 12, 10268−10279

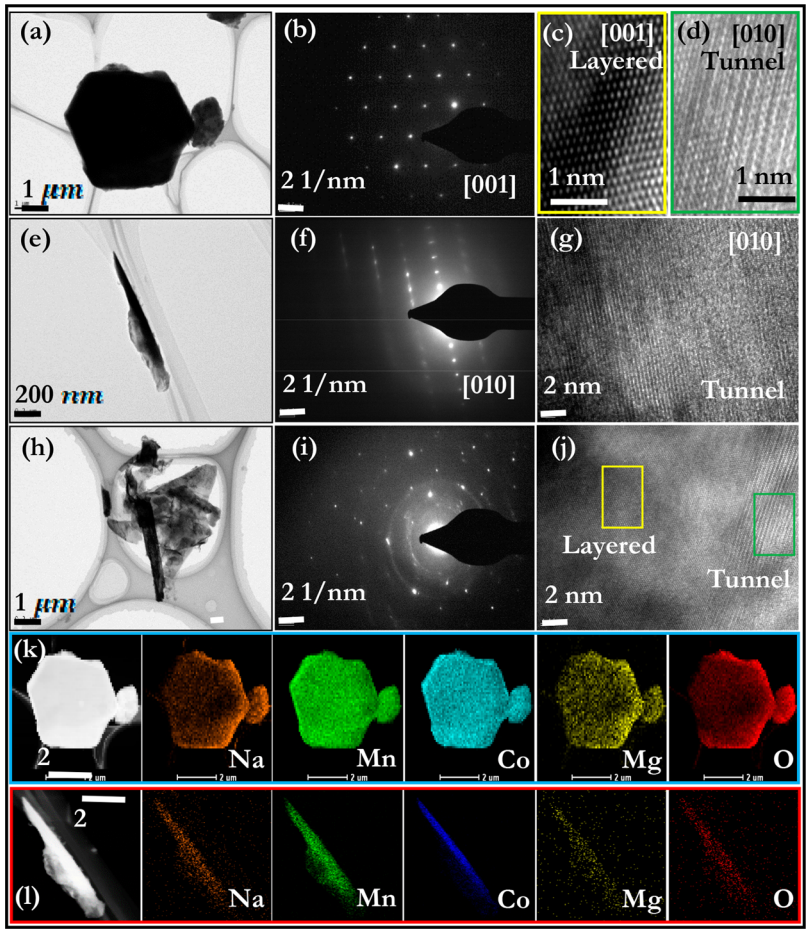

Figure 4. TEM image of (a) P2-layered particle and its (b) SAED pattern. (e) TEM of the tunnel structure. (f) SAED pattern of the tunnel structure. (g) HR-TEM of the tunnel structure. (h) TEM image of the layered tunnel intergrown structure. (i) SAED of the intergrown structure and its (j) HRTEM image. Yellow and green boxes represent the layered and tunnel structure, and its magnified views are provided in (c) layered and (d) tunnel. Elemental mapping of the (k) hexagonal layered particle and (l) needle-like tunnel structure.

Na).[59] The peak appearing above 4.2 V vs Na was due to the phase transition from P2 to O2, which is common for P2 layered oxides. At a higher voltage, more Na ions were extracted from the crystal lattice, resulting in a greater repulsive force among the electron shells of the adjacent O layers, which caused structural transitions.[38] The current peaks at high voltages were highly reversible during charge−discharge without any additional phase change. The Mn at lower voltages exhibited a large shift between the reduction and oxidation peaks owing to the Jahn−Teller-induced phase transition at high Na contents. In addition, the high-voltage peak corresponding to the P2−O2 phase transition was minimized after Mg doping. The presence of Mg reduced the slab length of the transition-metal layer, thereby increasing the interplanar distance between the two adjacent slabs and facilitating the smooth transport of alkali ions, even at a high voltage. This improvement was due to the bond strength of Mg−O, which was much higher than that of Co−O and endowed the insertion host with better stability, resulting in the high reversibility of the layered−tunnel structure compared with the pure layered sample.[55]

Figure 5b shows the galvanostatic charge−discharge cycling at a constant current of 100 mA g^{-1} within 1.5−4.3 V vs Na. The initial charge curve indicated a low capacity for both samples owing to the low Na content in the structure. The amount of Na extracted during the first desodiation process was calculated using Faraday's law.[60] The potential profiles exhibited two plateaus at 4.0 and 2.1 V vs Na, substantiating the CV results. Upon cycling, the pristine electrode exhibited a higher discharge capacity of 141 mAh g^{-1} at a current density of 85 mA g^{-1} and retained only 55.62% after 130 cycles. The layered−tunnel hybrid structure exhibited a slightly lower initial capacity (138 mAh g^{-1}) but exhibited better stability (71.19%) than the layered phase (Figure 5c). This capacity fading in the pristine electrode is attributed to the inevitable phase transition accompanied by a volume change at high voltages. In addition, the Jahn−Teller distortion and associated Mn dissolution at low voltages along with the high-voltage oxidative decomposition of the electrolyte cannot be ignored.[37,38] Figure S2 shows the voltage profiles of the cells cycled in the range of 2.0−4.5 V vs Na. The charge−discharge curves obtained for the MCM sample within this voltage range clearly indicated a suppressed P2−O2 phase transition above 4.2 V vs Na, confirming the significant role of the Mg doping. Thus, optimizing electrodes with stable performance and a high capacitance is a prerequisite for the development of high-performance NICs. The results suggest that a cutoff voltage of 1.5−4.3 V vs Na is appropriate for the battery-type electrode for the fabrication of high-performance NICs.

For the practical application of the NIC, high-rate electrochemical performance is a significant factor. Hence, charge−discharge tests were performed at different current

https://dx.doi.org/10.1021/acsami.9b19288
ACS Appl. Mater. Interfaces 2020, 12, 10268−10279

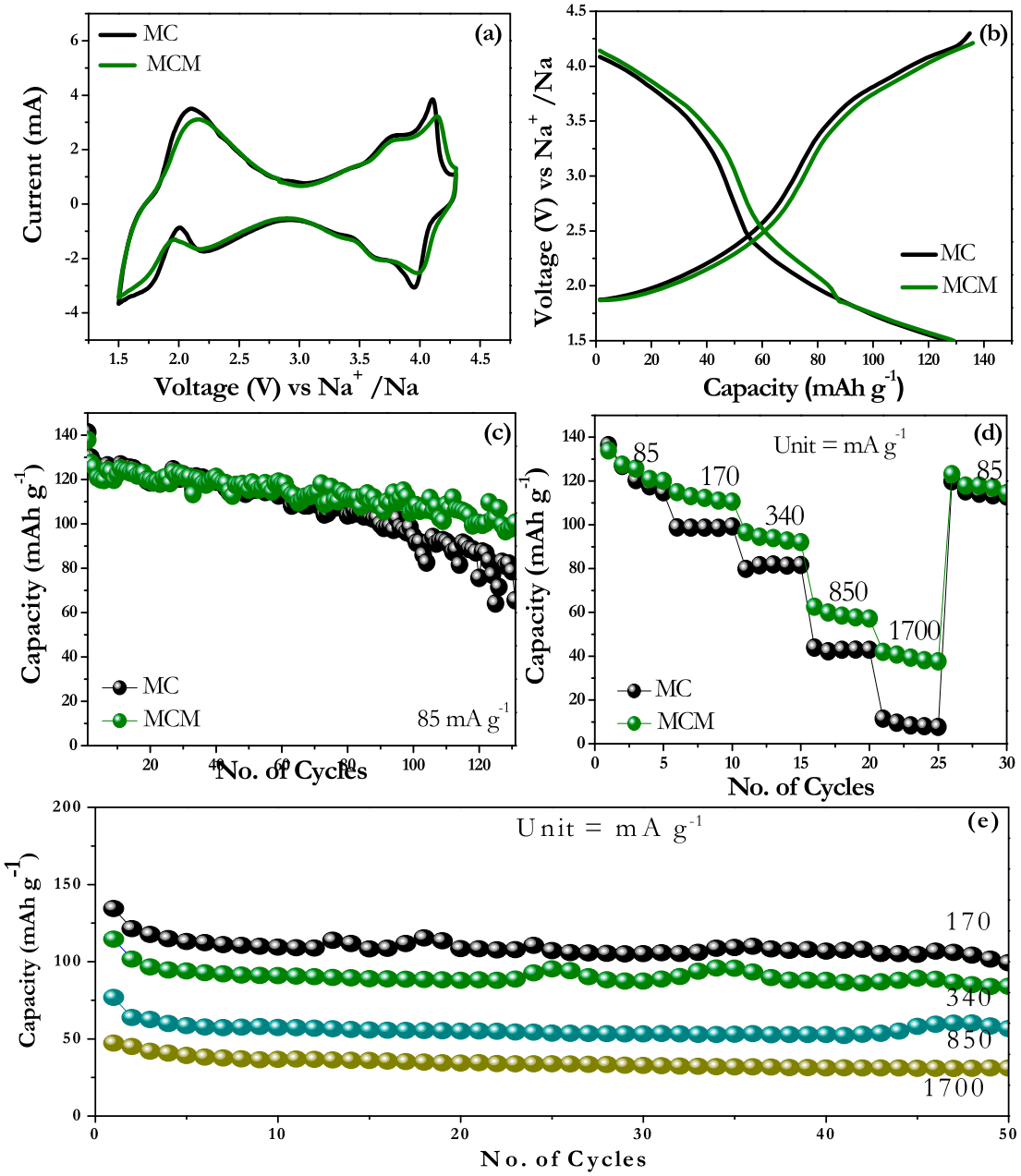

Figure 5. Comparison of the electrochemical performance of the MC and MCM samples. (a) CV curves. (b) charge−discharge curves. (c) Stability at 85 mA g^{-1}. (d) Rate performance. (e) Stability of the MCM sample at different current rates.

rates ranging from 85 to 1700 mA g^{-1} in the voltage range of 1.5−4.3 V vs Na. The results are shown in Figure 5d. The MC with the pure P2 phase exhibited discharge capacities of 136, 99, 80, 44, and 12 mAh g^{-1} at current densities of 85, 170, 340, 680, and 1700 mA g^{-1}, respectively. In comparison, the Mg-doped layered−tunnel hybrid structure exhibited a superior rate capability, with capacities of 134, 114, 96, 53, and 41 mAh g^{-1}, respectively. The hybrid cathode well recovered the original capacity, with 123 mAh g^{-1} at a current density of 85 mA g^{-1}, whereas the pristine structure recovered a capacity of 119 mAh g^{-1}. When the discharge capacity at a lower current rate (85 mA g^{-1}) was assumed to be 100%, the normalized capacity of the pristine cathode was 72.4%, 58.86%, and 32.19% at 170, 340, and 680 mA g^{-1} and reached a very low value of 8.4% at a higher current rate of 1700 mA g^{-1}. In contrast, the Mg-doped layered−tunnel hybrid cathode exhibited significantly higher values of the normalized capacity: 85%, 71.6%, 47%, and 30%, respectively. The MCM sample shows better stability for 50 cycles irrespective of the applied current rate as shown in Figure 5e. This is attributed to the combined effects of Mg doping and formation of the tunnel-like structure with 3D pathways for Na-ion migration.[61] Partial substitution of Mg^{2+} for toxic and expensive Co ions reduced the TM−O bond length, thereby increasing the bond strength.[55] In addition, this prevented Na^+/vacancy and phase gliding during Na extraction. Furthermore, the tunnel-shaped cathode had a 3D alkali-ion diffusion path with a wide *d* spacing, which was far more effective than the 2D pathways in previously reported layered cathode materials.[62,63] Further, the cycling stability of different concentrations of Mg-doped samples is provided in Figure S3. When the concentration of electrochemically inactive Mg is increased, the electrochemi-

https://dx.doi.org/10.1021/acsami.9b19288
ACS Appl. Mater. Interfaces 2020, 12, 10268−10279

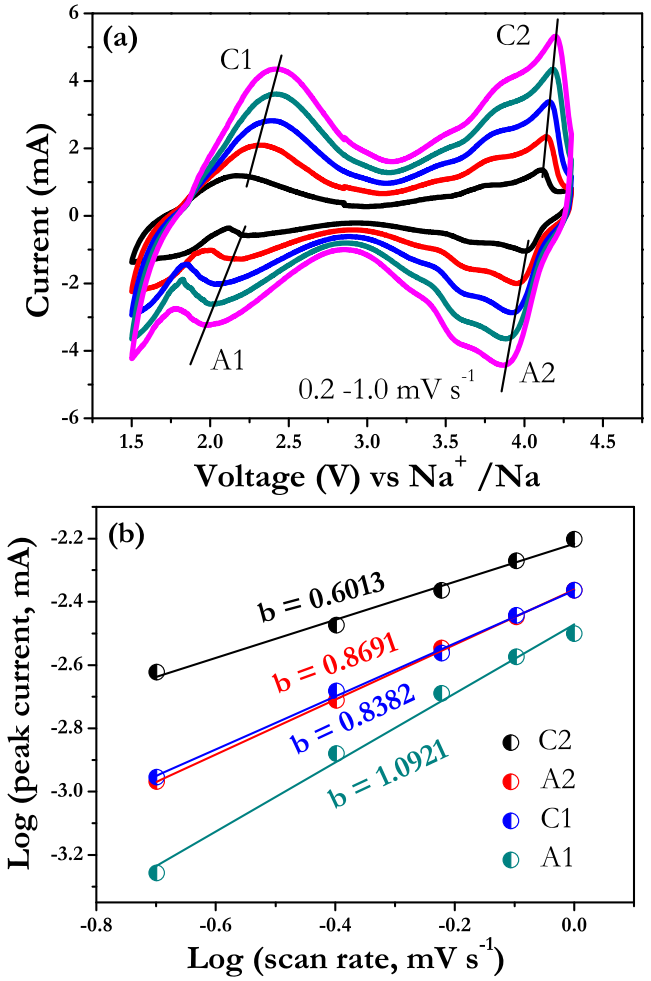

Figure 6. (a) CV curves of MCM at various scan rates from 0.2 to 1.0 mV s^{-1}. (b) Peak current vs scan rate plots to determine the *b* value of the anodic and cathodic peaks.

cally active Co is simultaneously decreased, leading to lower capacity. Retention of 0.02 Mg doped is better than that of other samples as mentioned earlier. This confirms that the optimal ratio of Co and Mg is essential to improve the electronic conductivity and structural stability of the cathode. Ex-situ XRD analysis is carried out for both MC and MCM after charging to 4.2 V at 85 mA g^{-1} to study the P2−O2 phase change. Both samples have additional peaks at 12° and 25° attributed to the appearance of hydrated peaks formed upon water intercalation during measurement. For the case of the MC sample, the major peaks of the P2 structure disappear and the onset of additional peaks at 22° indicate O2 stacking, whereas the major peaks of the P2 phase are well preserved for the MCM sample (Figure S4).

Kinetic analysis was carried out using the cyclic voltammetry method. The CV curves of the MCM cathode at various scan rates are shown in Figure 6a. Two pairs of redox peaks corresponding to Mn and Co redox are observed. The peaks shift slightly with increasing scan rates, indicating excellent kinetics. A related analysis is taken to investigate the relationship between peak current and scan rate according to equation[64]

$$i = av^b$$

The value of $b = 0.5$ indicates semi-infinite linear diffusion-controlled charge storage, whereas $b = 1$ indicates capacitive-dominated charge storage. The *b* value can be obtained by plotting $\log(i)$ vs $\log(v)$ as shown in Figure 6b. Here the value of *b* is close to 1, indicating a capacitive-dominated process. Figure 7 shows the impedance spectra of MC and MCM before and after cycling fitted using an equivalent circuit provided as the inset. The corresponding parameters are provided in Table S3. In both figures, the value of resistance for MCM is lower than the MC sample resulting from the biphasic structure of MCM.

For the fabrication of a NIC, the half-cell performance of commercial AC was studied in the CR2032 coin cell using Na metal as a counter electrode, Figure S5. The electrochemical performance was evaluated under similar testing conditions. Charge−discharge tests were conducted in the voltage window of 1.0−3.5 V vs Na at a current density of 100 mA g^{-1} to evaluate the capacitive performance of the AC in the lower voltage window. The AC electrode exhibited a reversible capacity of 80 mAh g^{-1} with good stability over 50 cycles. The linear variation of the charge−discharge curve with respect to the potential indicated ideal capacitor behavior, i.e., a non-Faradaic process. Owing to the excellent electrochemical performance of MCM in the Na half-cell assembly, we fabricated a full cell, i.e., the NIC coupled with AC. The charge-storage behavior differed between the electrodes; thus,

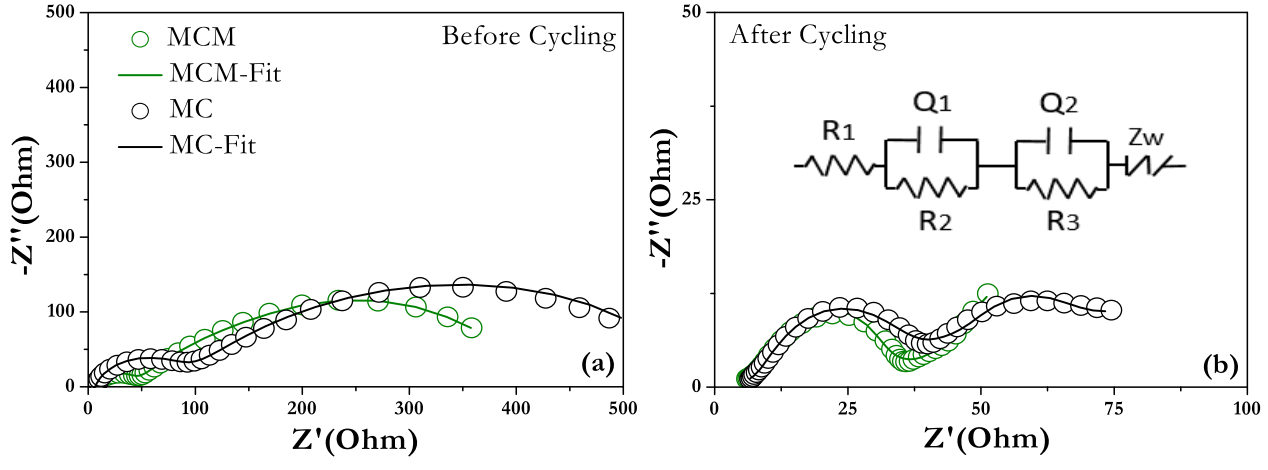

Figure 7. Nyquist plot of MC and MCM obtained before and after cycling.

https://dx.doi.org/10.1021/acsami.9b19288
ACS Appl. Mater. Interfaces 2020, 12, 10268−10279

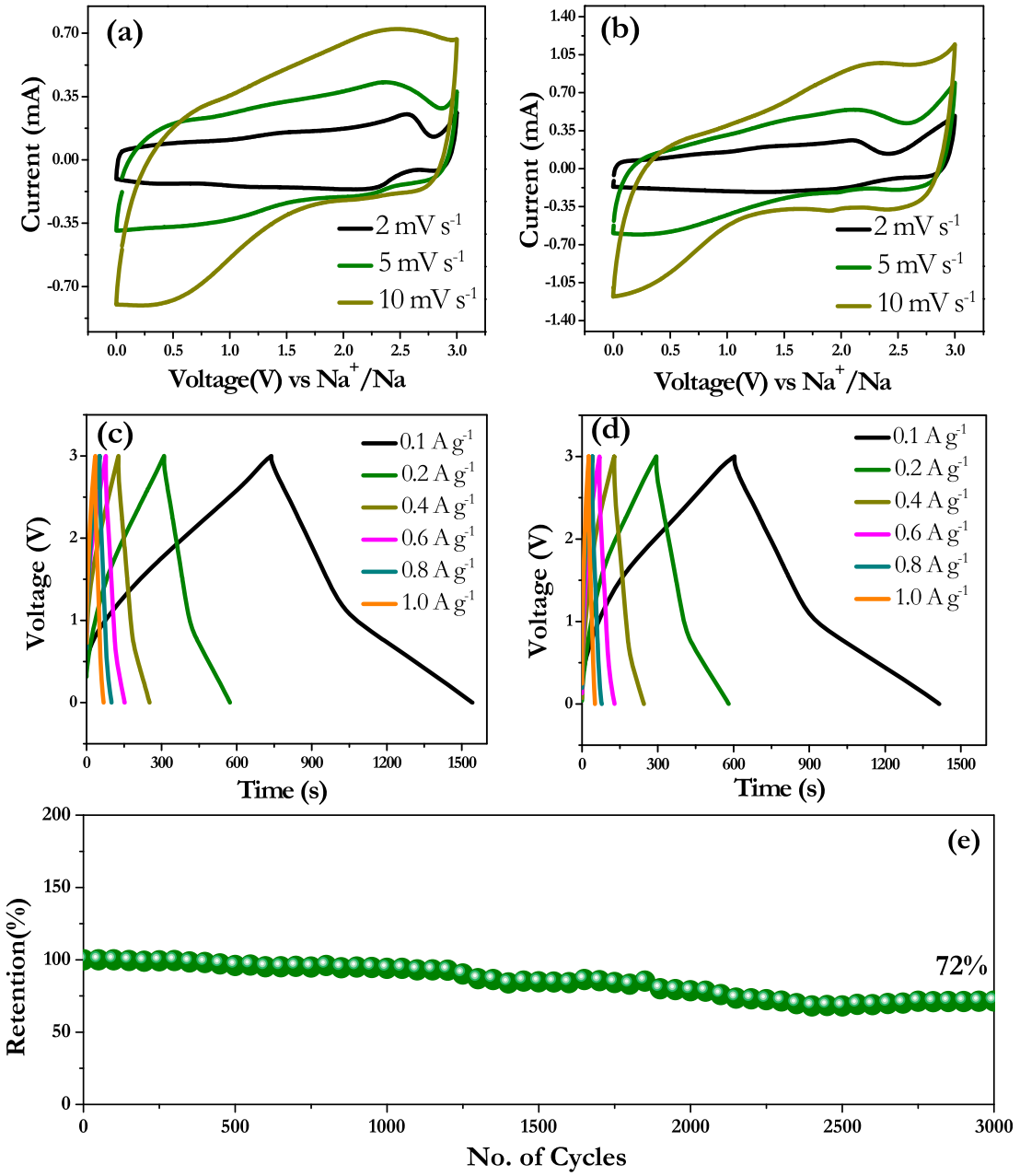

Figure 8. Electrochemical performance of the MCM//AC NIC. (a) CV curves measured with a cathode:anode ratio of 1:1. (b) CV curves measured with a cathode:anode ratio of 1:2. (c) Charge−discharge curves measured with a cathode:anode ratio of 1:1. (d) Charge−discharge curves measured with a cathode:anode ratio of 1:2. (e) Retention of MCM//AC SIC measured at 1A g^{-1}.

the applied current was divided according to the individual capacities of the electrodes.[26] Hence, the mass balance of the electrodes is necessary to realize the maximum potential of the NIC. The AC stored charge via the surface adsorption/desorption of ClO_4^- ions, whereas the MCM served as a Na-intercalation/deintercalation host. We carefully considered the average voltage and capacity of both electrodes in a half-cell configuration and assembled the NIC with two different mass ratios (1:1 and 1:2). The voltage range of the NIC was fixed at 0−3 V to avoid electrolyte decomposition at higher voltages. The commercial EDLC using an organic electrolyte has a potential window limitation of 2.7 V.[65] The CV (Figure 8a and 8b) was performed in this voltage range at different scan rates (2, 5, and 10 mV s^{-1}). The CV curve exhibited asymmetric behavior at lower scan rates owing to the major contribution of the Faradaic component and the small contribution of the non-Faradaic charge storage. At higher scan rates, the CV curves became rectangular with the dominance of capacitor-type behavior, i.e., a minor contribution from the battery-type electrode. Other than the area under the CV curve, there was no significant difference between the MC-based and the MCM-based NICs.[25] The energy and power densities were calculated using the galvanostatic charge−discharge curves by considering the total mass of the active materials. The charge−discharge curves for both mass ratios are shown in Figure 8c and 8d. The asymmetrical nature of the curve indicates the combination of two different charge-storage mechanisms.[27] Long-term cyclic stability is a very important factor for practical application of NICs. Hence, we evaluated the cyclic stability of the AC//MCM hybrid capacitor at 1 A g^{-1}. The

https://dx.doi.org/10.1021/acsami.9b19288
ACS Appl. Mater. Interfaces 2020, 12, 10268−10279

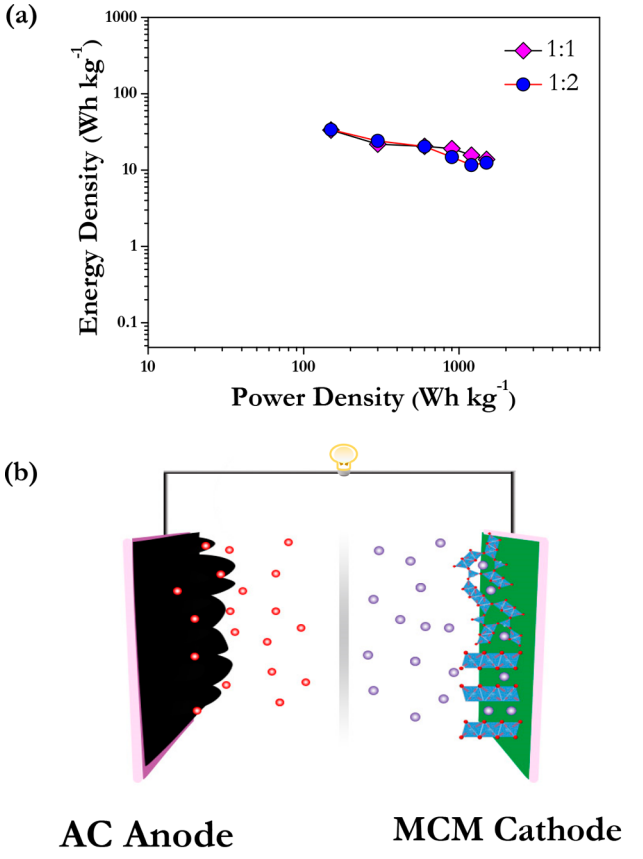

Figure 9. (a) Ragone plot of the MCM//ac hybrid capacitor. (b) Schematic of the hybrid capacitor setup.

values were normalized for convenience; for example, when the initial value of 14 Wh kg^{-1} was considered as 100%, the cell retained >72% of its energy density after 3000 cycles, indicating the excellent stability of this novel configuration (Figure 8e). The energy and power densities were calculated using the following equations[67,68]

$$P = \frac{i\,(\mathrm{A}) \times V}{m\,(\mathrm{mg}) \times 10^{-6}} \text{ and } E = \frac{P \times \Delta t}{3600}$$

where i represents the applied current (A), t represents the discharge time (s), m represents the total weight of the active material in both electrodes, and V represents the working potential of the cell, which was determined using the galvanostatic charge−discharge curves. As shown in Figure 9a, the sample with a 1:1 mass ratio exhibited an energy density of 34 Wh kg^{-1} at a power density of 150 W kg^{-1}. This value is similar to that of the commercial AC//$Li_4Ti_2O_{12}$ (36 Wh kg^{-1}).[69] Further, the variation in the mass loading did not affect the energy density or power capability of the NICs, as indicated by the Ragone plot. Figure 9b shows the schematic of the NIC. The performance of the novel hybrid capacitor was higher than that of most previously reported LIC and NIC, as shown in Table S4. The performance of this family of layered oxides can be further improved by fabricating highly conducting composites for better conductivity and as a supporting matrix.[13] In addition, replacing the commercial AC with tailored carbonaceous materials can significantly enhance the energy and power capability of the system.[70]

EIS is a powerful tool that can provide quantitative information regarding the surface stability, charge-transfer resistance, and diffusion kinetics of Na ions within the bulk material of the cathode.[66] Hence, we performed EIS for NIC before and after cycling at 1 A g^{-1}, and the corresponding Nyquist plot is shown in Figure S6. The Nyquist plot exhibited a semicircle in the high-to-medium-frequency region, accompanied by a sloping line in the high-frequency region. The former corresponds to charge transfer resistance, while the latter is diffusion-related impedance. The change in the diameter of the semicircular arc after cycling is negligible due to the lower surface resistance at higher voltages. The change of the sloping line was due to the suppressed high-voltage phase transition at a low Na content.[59] This demonstrates the superiority of this system compared to reported works.

CONCLUSION

A high-energy NIC was fabricated using a novel layered−tunnel hybrid cathode as an insertion host and commercial AC as a supercapacitor component. The hybrid cathode was synthesized via the conventional sol−gel method and characterized using various analytical techniques to confirm the hybrid nature and its impact on the Na-storage performance. The fabricated NIC exhibited a very high energy density of 34 Wh kg^{-1} with a superior cycling stability of 72% after 3000 cycles. These results are significant for the field of NICs, as they provide a new cost-effective method for designing high-capacity cathodes for high-performance energy-storage devices.

ASSOCIATED CONTENT

Supporting Information

The Supporting Information is available free of charge at https://pubs.acs.org/doi/10.1021/acsami.9b19288.

XRD and cyclability of doped samples, charge−discharge at different cutoff voltages, ex-situ XRD at charged state, EIS of NIC, half-cell studies of ac, Rietveld parameters, resistance values calculated by fitting the Nyquist plot, comparison table with other reported works (PDF)

AUTHOR INFORMATION

Corresponding Author

Yun-Sung Lee − *Department of Advanced Chemicals and Engineering, Chonnam National University, Gwang-ju 61186, Republic of Korea;* orcid.org/0000-0002-6676-2871; Email: leeys@chonnam.ac.kr

Authors

Hyun-Jae Kim − *Department of Advanced Chemicals and Engineering, Chonnam National University, Gwang-ju 61186, Republic of Korea*

Hari Vignesh Ramasamy − *Department of Advanced Chemicals and Engineering, Chonnam National University, Gwang-ju 61186, Republic of Korea;* orcid.org/0000-0002-8241-2441

Gang-Hyeon Jeong − *Department of Advanced Chemicals and Engineering, Chonnam National University, Gwang-ju 61186, Republic of Korea*

Vanchiappan Aravindan − *Department of Chemistry, Indian Institute of Science Education and Research (IISER), Tirupati 517507, India;* orcid.org/0000-0003-1357-7717

Complete contact information is available at:

https://dx.doi.org/10.1021/acsami.9b19288
ACS Appl. Mater. Interfaces 2020, 12, 10268−10279

https://pubs.acs.org/10.1021/acsami.9b19288

Author Contributions

‡H.J.K. and H.V.R. contributed equally to this work.

Notes

The authors declare no competing financial interest.

■ ACKNOWLEDGMENTS

The authors gratefully acknowledge the financial support from a National Research Foundation of Korea (NRF) grant funded by the Korean government (Ministry of Science, ICT & Future Planning) (No. 2019R1A4A2001527).

■ REFERENCES

(1) Yang, Z.; Zhang, J.; Kintner-Meyer, M. C. W.; Lu, X.; Choi, D.; Lemmon, J. P.; Liu, J. Electrochemical Energy Storage for Green grid. *Chem. Rev.* **2011**, *111*, 3577−3613.

(2) Li, X.; Colclasure, A. M.; Finegan, D. P.; Ren, D.; Shi, Y.; Feng, X.; Cao, L.; Yang, Y.; Smith, K. Degradation Mechanisms of High Capacity 18650 cells containing Si-Graphite Anode and Nickel-rich NMC Cathode. *Electrochim. Acta* **2019**, *297*, 1109−1120.

(3) Grosjean, C.; Miranda, P. H.; Perrin, M.; Poggi, P. Assessment of world lithium resources and consequences of their geographic distribution on the expected development of the electric vehicle industry. *Renewable Sustainable Energy Rev.* **2012**, *16*, 1735−1744.

(4) Li, W. J.; Han, C.; Wang, W.; Gebert, F.; Chou, S. L.; Liu, H. K.; Zhang, X.; Dou, S. X. Commercial Prospects of Existing Cathode Materials for Sodium Ion Storage. *Adv. Energy Mater.* **2017**, *7*, 1700274.

(5) Pan, H.; Hu, Y. S.; Chen, L. Room-Temperature Stationary Sodium-ion Batteries for Large-Scale Electric Energy storage. *Energy Environ. Sci.* **2013**, *6*, 2338−2360.

(6) Kim, Y.; Ha, K.-H.; Oh, S. M.; Lee, K. T. High-Capacity Anode Materials for Sodium-Ion. *Chem. - Eur. J.* **2014**, *20*, 11980−11992.

(7) Kotz, R.; Carlen, M. Principles and applications of Caps. *Electrochim. Acta* **2000**, *45*, 2483−2498.

(8) Amatucci, G. G.; Badway, F.; Du Pasquier, A.; Zheng, T. An Asymmetric Hybrid Nonaqueous Energy Storage Cell. *J. Electrochem. Soc.* **2001**, *148*, A930−A939.

(9) Ronsmans, J.; Lalande, B. Combining Energy with Power: Lithium-ion Capacitors, International Conference on Electrical Systems for Aircraft, Railway, Ship Propulsion and Road Vehicles (ESARS), Aachen *IEEE*, **2015**, 1−4.

(10) Yin, J.; Qi, L.; Wang, H. Sodium Titanate Nanotubes as Negative Electrode Materials for Sodium-ion Capacitors. *ACS Appl. Mater. Interfaces* **2012**, *4*, 2762−2768.

(11) Yun, Y. S.; Cho, S. Y.; Kim, H.; Jin, H. J.; Kang, K. Ultra-Thin Hollow Carbon Nanospheres for Pseudocapacitive Sodium-Ion Storage. *ChemElectroChem* **2015**, *2*, 359−365.

(12) Wang, H.; Zhu, C.; Chao, D.; Yan, Q.; Fan, H. J. Nonaqueous Hybrid Lithium Ion and Sodium Ion Capacitors. *Adv. Mater.* **2017**, *29*, 1702093.

(13) Lim, E.; Kim, H.; Jo, C.; Chun, J.; Ku, K.; Kim, S.; Lee, H. I.; Nam, I. S.; Yoon, S.; Kang, K.; Lee, J. Advanced Hybrid Supercapacitor based on a Mesoporous Niobium Pentoxide/Carbon as High-Performance Anode. *ACS Nano* **2014**, *8*, 8968−8978.

(14) Li, Y.; Wang, H.; Wang, L.; Mao, Z.; Wang, R.; He, B.; Gong, Y.; Hu, X. Mesopore-Induced Ultrafast Na^+- Storage in T-Nb_2O_5/Carbon Nanofiber Films toward Flexible High Power Na-Ion Capacitors. *Small* **2019**, *15*, 1804539.

(15) Wasiński, K.; Półrolniczak, P.; Walkowiak, M. Proof-of-Concept Study of a New Type Sodium-ion Hybrid Electrochemical Capacitor with Organic Electrolyte. *Electrochim. Acta* **2018**, *259*, 850−854.

(16) Mao, Z.; Wang, R.; He, B.; Gong, Y.; Wang, H. Large-Area, Uniform, Aligned Arrays of $Na_3((VO)_2(PO_4)_2F$ on Carbon Nanofiber for Quasi Solid State Sodium ion Hybrid Capacitor. *Small* **2019**, *15*, 1902466.

(17) Gao, S.; Zhao, J.; Zhao, Y.; Wu, Y.; Zhang, X.; Wang, L.; Liu, X.; Rui, Y.; Xu, J. Na_2CoSiO_4 as a novel positive electrode material for sodium-ion capacitors. *Mater. Lett.* **2015**, *158*, 300−303.

(18) Wang, X.; Li, G.; Chen, Z.; Augustyn, V.; Ma, X.; Wang, G.; Dunn, B.; Lu, Y. High-Performance Supercapacitors Based on Nanocomposites of Nb_2O_5 Nanocrystals and Carbon Nanotubes. *Adv. Energy Mater.* **2011**, *1*, 1089−1093.

(19) Chen, Z.; Augustyn, V.; Jia, X.; Xiao, Q.; Dunn, B.; Lu, Y. High Performance Sodium ion Pseudocapacitors based on Hierarchially Porous Nanowire Composites. *ACS Nano* **2012**, *6*, 4319−4327.

(20) Ding, R.; Qi, L.; Wang, H. An Investigation of Spinel $NiCo_2O_4$ as Anode for Na-ion Capacitors. *Electrochim. Acta* **2013**, *114*, 726−732.

(21) Li, H.; Zhu, Y.; Dong, S.; Shen, L.; Chen, Z.; Zhang, X.; Yu, G. Self-Assembled Nb_2O_5 Nanosheets for High Energy-High Power Sodium Ion Capacitors. *Chem. Mater.* **2016**, *28*, 5753−5760.

(22) Aravindan, V.; Shubha, N.; Ling, W. C.; Madhavi, S. Constructing High Energy Density Non-Aqueous Li-ion Capacitors using Monoclinic TiO_2-B Nanorods as Insertion Host. *J. Mater. Chem. A* **2013**, *1*, 6145−6151.

(23) Xu, D.; Chao, D.; Wang, H.; Gong, Y.; Wang, R.; He, B.; Hu, X.; Fan, H. J. *Flexible Quasi Solid State Sodium Ion Capacitors Developed using 2D Metal-Organic Framework Array as reactor* **2018**, *8*, 1702769.

(24) Chaturvedi, A.; Hu, P.; Long, Y.; Kloc, C.; Madhavi, S.; Aravindan, V. *Scr. Mater.* **2019**, *161*, 54−57.

(25) Karthikeyan, K.; Kim, S. H.; Kim, K. J.; Lee, S. N.; Lee, Y. S. Low cost, eco-friendly Layered $Li_{1.2}(Mn_{0.32}Ni_{0.32}Fe_{0.16})O_2$ Nanoparticles for Hybrid Supercapacitor Applications. *Electrochim. Acta* **2013**, *109*, 595−601.

(26) Ramasamy, H. V.; Senthilkumar, B.; Barpanda, P.; Lee, Y. S. Superior Potassium-ion Hybrid Capacitor Based on Novel P3-type Layered $K_{0.45}Mn_{0.5}Co_{0.5}O_2$ as High Capacity Cathode. *Chem. Eng. J.* **2019**, *368*, 235−243.

(27) Karthikeyan, K.; Amaresh, S.; Aravindan, V.; Kim, H.; Kang, K. S.; Lee, Y. S. Unveiling Organic-Inorganic Hybrids as a Cathode Material for High Performance Lithium-ion Capacitors. *J. Mater. Chem. A* **2013**, *1*, 707−714.

(28) Karthikeyan, K.; Amaresh, S.; Kim, K. J.; Kim, S. H.; Chung, K. Y.; Cho, B. W.; Lee, Y. S. A High Performance Hybrid Capacitor with Li_2CoPO_4F Cathode and Activated Carbon Anode. *Nanoscale* **2013**, *5*, 5958−5964.

(29) Zou, K.; Cai, P.; Liu, C.; Li, J.; Gao, X.; Xu, L.; Zou, G.; Hou, H.; Liu, Z.; Ji, X. A Kinetically Well-Matched Full-Carbon Sodium-ion Capacitor. *J. Mater. Chem. A* **2019**, *7*, 13540−13549.

(30) Wu, X.; Guo, J.; Wang, D.; Zhong, G.; McDonald, M. J.; Yang, Y. P2-type $Na_{0.66}Ni_{0.33-x}Zn_xMn_{0.67}O_2$ as New High-Voltage Cathode Materials for Sodium-ion Batteries. *J. Power Sources* **2015**, *281*, 18−26.

(31) Li, Y.; Yang, Z.; Xu, S.; Mu, L.; Gu, L.; Hu, Y. S.; Li, H.; Chen, L. Air-Stable Copper-Based P2-$Na_{7/9}Cu_{2/9}Fe_{1/9}Mn_{2/3}O_2$ as a New Positive Electrode Material for Sodium-Ion Batteries. *Adv. Sci.* **2015**, *2*, 1500031.

(32) Wang, L.; Sun, Y.-G.; Hu, L.-L.; Piao, J.-Y.; Guo, J.; Manthiram, A.; Ma, J.; Cao, A.-M. Copper-Substituted $Na_{0.67}Ni_{0.3-x}Cu_xMn_{0.7}O_2$ Cathode Materials for Sodium-Ion Batteries with Suppressed P2-O2 Phase Transition. *J. Mater. Chem. A* **2017**, *5*, 8752−8761.

(33) Delmas, C.; Fouassier, C.; Hagenmuller, P. Structural Classification and Properties of the Layered Oxides. *Physica B+C* **1980**, *99*, 81−85.

(34) Su, H.; Jaffer, S.; Yu, H. Transition Metal Oxides for Sodium-ion Batteries. *Energy Storage Mater.* **2016**, *5*, 116−131.

(35) Parant, J. P.; Olazcuaga, R.; Devalette, M.; Fouassier, C.; Hagenmuller, P. Sur Quelques Nouvelles Phases de Formule Na_xMnO_2 ($x \leq 1$). *J. Solid State Chem.* **1971**, *3*, 1−11.

(36) Ortiz-Vitoriano, N.; Drewett, N. E.; Gonzalo, E.; Rojo, T. High Performance Manganese-based Layered Oxide Cathodes: Overcoming the Challenges of Sodium Ion Batteries. *Energy Environ. Sci.* **2017**, *10*, 1051−1074.

(37) Li, X.; Ma, X.; Su, D.; Liu, L.; Chisnell, R.; Ong, S. P.; Chen, H.; Toumar, A.; Idrobo, J. C.; Lei, Y.; Bai, J.; Wang, F.; Lynn, J. W.; Lee, Y. S.; Ceder, G. Direct Visualization of the Jahn-Teller Effect Coupled to Na Ordering in $Na_{5/8}MnO_2$. *Nat. Mater.* **2014**, *13*, 586−592.
(38) Wang, P. F.; You, Y.; Yin, Y. X.; Wang, Y. S.; Wan, L. J.; Gu, L.; Guo, Y. G. Suppressing the P2−O2 Phase Transition of $Na_{0.67}Mn_{0.67}Ni_{0.33}O_2$ by Magnesium Substitution for Improved Sodium-Ion Batteries. *Angew. Chem., Int. Ed.* **2016**, *55*, 7445−7449.
(39) Ramasamy, H. V.; Kaliyappan, K.; Thangavel, R.; Aravindan, V.; Kang, K.; Kim, D. U.; Park, Y.; Sun, X.; Lee, Y.-S. Cu-doped P2-$Na_{0.5}Ni_{0.33}Mn_{0.67}O_2$ Encapsulated with MgO as a Novel High Voltage Cathode with Enhanced Na-Storage Properties. *J. Mater. Chem. A* **2017**, *5*, 8408−8415.
(40) Qu, J.; Sheng, T.; Wu, Z.; Chen, T.; Chen, H.; Yang, Z.; Guo, X.; Li, J.; Zhong, B.; Dou, X. Unexpected effects of zirconium-doping in the high performance sodium manganese-based layer-tunnel cathode. *J. Mater. Chem. A* **2018**, *6*, 13934−13942.
(41) Wang, Q. C.; Qiu, Q. Q.; Xiao, N.; Fu, Z. W.; Wu, X. J.; Yang, X. Q.; Zhou, Y. N. Tunnel-Structured $Na_{0.66}[Mn_{0.66}Ti_{0.34}]O_{2-x}F_x$ ($x < 0.1$) Cathode for High Performance Sodium-ion Batteries. *Energy Storage Mater.* **2018**, *15*, 1−7.
(42) Gao, G.; Tie, D.; Ma, H.; Yu, H.; Shi, S.; Wang, B.; Xu, S.; Wang, L.; Zhao, Y. Interface-rich mixed P2 + T phase $Na_xCo_{0.1}Mn_{0.9}O_2$($0.44 \leq x \leq 0.7$) toward Fast and High Capacity Sodium Storage. *J. Mater. Chem. A* **2018**, *6*, 6675−6684.
(43) Qu, J.; Wang, D.; Yang, Z.; Wu, Z.; Qiu, L.; Guo, X.; Li, J.; Zhong, B.; Chen, X.; Dou, S. Ion-Doping Site Variation Induced Composite Cathode Adjustment: A Case Study of Layer-Tunnel $Na_{0.6}MnO_2$ and Mg^{2+} Doping at Na/Mn site. *ACS Appl. Mater. Interfaces* **2019**, *11*, 26938−26945.
(44) Keller, M.; Buchholz, D.; Passerini, S. Layered Na-Ion Cathodes with Outstanding Performance Resulting from the Synergetic Effect of Mixed P- and O-Type Phases. *Adv. Energy Mater.* **2016**, *6*, 1−11.
(45) Wang, D.; Chen, H.; Zheng, X.; Qiu, L.; Qu, J.; Wu, Z.; Zhong, Y.; Xiang, W.; Zhong, B.; Guo, X. Simultaneous Component Ratio and Particle Size Optimization for High Performance and High Tap Density P2/P3 Composite Cathode of Sodium ion Batteries. *ChemElectroChem* **2019**, *6*, 5155−5161.
(46) Guo, S.; Liu, P.; Yu, H.; Zhu, Y.; Chen, M.; Ishida, M.; Zhou, H. A layered P2- and O3-type composite as a high-energy cathode for rechargeable sodium-ion batteries. *Angew. Chem., Int. Ed.* **2015**, *54*, 5894−5899.
(47) Chen, H.; Wu, Z.; Zheng, Z.; Chen, T.; Guo, X.; Li, J.; Zhong, B. Tuning the Component Ratio and Corresponding Sodium Storage Properties of Layer Tunnel Hybrid $Na_{0.6}Mn_{1-x}Ni_xO_2$ Cathode by a Simple Cationic Ni^{2+} doping strategy. *Electrochim. Acta* **2018**, *273*, 63−70.
(48) Chen, T. R.; Sheng, T.; Wu, Z. G.; Li, J. T.; Wang, E. H.; Wu, C. J.; Li, H. T.; Guo, X. D.; Zhong, B. H.; Huang, L.; Sun, S. G. Cu^{2+} Dual-Doped Layer-Tunnel Hybrid $Na_{0.6}Mn_{1-x}Cu_xO_2$ as a Cathode of Sodium-Ion Battery with Enhanced Structure Stability, Electrochemical Property, and Air Stability. *ACS Appl. Mater. Interfaces* **2018**, *10*, 10147−10156.
(49) Xiao, Y.; Zhu, Y. F.; Xiang, W.; Wu, Z. G.; Li, Y. C.; Lai, J.; Li, S.; Wang, E.; Yang, Z. G.; Xu, C. L.; Zhong, B. H.; Guo, X. D. Deciphering Abnormal Layered Tunnel Heterostructure Induced via Chemical Substitution for Sodium Oxide Cathode. *Angew. Chem.* **2020**, *132*, 1507.
(50) Xiao, Y.; Wang, P. F.; Yin, Y. X.; Zhu, Y. F.; Yang, X.; Zhang, X. D.; Wang, Y.; Guo, X. D.; Zhong, B. H.; Guo, Y. G. A Layered−Tunnel Intergrowth Structure for High-Performance Sodium-Ion Oxide Cathode. *Adv. Energy Mater.* **2018**, *8*, 1800492.
(51) Li, T.; Yu, D.; Liu, J.; Wang, F. Atomic Pt promoted N-Doped Carbon as Novel Negative Electrode for Li ion Batteries. *ACS Appl. Mater. Interfaces* **2019**, *11*, 37559−37566.
(52) Wu, Z. G.; Li, J. T.; Zhong, Y. J.; Guo, X. D.; Huang, L.; Zhong, B. H.; Agyeman, D. A.; Lim, J. M.; Kim, D. H.; Cho, M. H.; Kang, Y. M. Mn-Based Cathode with Synergetic Layered-Tunnel Hybrid Structures and Their Enhanced Electrochemical Performance in Sodium Ion Batteries. *ACS Appl. Mater. Interfaces* **2017**, *9*, 21267−21275.
(53) Thangavel, R.; Kaliyappan, K.; Ramasamy, H. V.; Sun, X.; Lee, Y. S. Engineering the Pores of Biomass Derived Carbon: Insights for Achieving Ultrahih Stability at High Power in High Energy Supercapacitors. *ChemSusChem* **2017**, *10*, 2805−2815.
(54) Ding, J. J.; Zhou, Y. N.; Sun, Q.; Yu, X. Q.; Yang, X. Q.; Fu, Z. W. Electrochemical Properties of P2-phase $Na_{0.74}CoO_2$ Compounds as Cathode Material for Rechargeable Sodium-ion Batteries. *Electrochim. Acta* **2013**, *87*, 388−393.
(55) Wen, Y.; Fan, J.; Shi, C.; Dai, P.; Hong, Y.; Wang, R.; Wu, L.; Zhou, Z.; Li, J.; Huang, L.; Sun, S. G. Probing into the Working Mechanism of Mg versus Co in Enhancing the Electrochemical Performance of P2-Type Layered Composite for Sodium-ion Batteries. *Nano Energy* **2019**, *60*, 162−170.
(56) Ramasamy, H. V.; Kaliyappan, K.; Thangavel, R.; Seong, W. M.; Kang, K.; Chen, Z.; Lee, Y.-S. Efficient Method of Designing Stable Layered Cathode Material for Sodium Ion Batteries Using Aluminum Doping. *J. Phys. Chem. Lett.* **2017**, *8*, 5021−5030.
(57) Zhou, Y. N.; Wang, P. F.; Zhang, X. D.; Huang, L. B.; Wang, W. P.; Yin, Y. X.; Xu, S.; Guo, Y. G. Air-Stable and High-Voltage Layered P3-Type Cathode for Sodium-Ion Full Battery. *ACS Appl. Mater. Interfaces* **2019**, *11*, 24184−24191.
(58) Wang, P.; Yao, H.; Liu, X.; Yin, Y.; Zhang, J.; Wen, Y.; Yu, X.; Gu, L.; Guo, Y. Na^+/vacancy Disordering Promises High-rate Na-ion. *Batteries* **2018**, *4*, eaar6018.
(59) Chen, X.; Zhou, X.; Hu, M.; Liang, J.; Wu, D.; Wei, J.; Zhou, Z. Stable Layered P3/P2 $Na_{0.66}Co_{0.5}$ $Mn_{0.5}O_2$ Cathode Materials for Sodium-ion Batteries. *J. Mater. Chem. A* **2015**, *3*, 20708−20714.
(60) Martinez De Ilarduya, J.; Otaegui, L.; López del Amo, J. M.; Armand, M.; Singh, G. NaN_3 Addition, a Strategy to Overcome the Problem of Sodium Deficiency in P2-$Na_{0.67}[Fe_{0.5}Mn_{0.5}]O_2$ Cathode for Sodium-ion Battery. *J. Power Sources* **2017**, *337*, 197−203.
(61) Shi, W. J.; Yan, Y. W.; Chi, C.; Ma, X. T.; Zhang, D.; Xu, S. D.; Chen, L.; Wang, X. M.; Liu, B. S. Fluorine anion doped $Na_{0.44}MnO_2$ with layer-tunnel hybrid structure as advanced cathode for sodium ion batteries. *J. Power Sources* **2019**, *427*, 129−137.
(62) Alvarado, J.; Ma, C.; Wang, S.; Nguyen, K.; Kodur, M.; Meng, Y. S. Improvement of the Cathode Electrolyte Interphase on P2-$Na_{2/3}Ni_{1/3}Mn_{2/3}O_2$ by Atomic Layer Deposition. *ACS Appl. Mater. Interfaces* **2017**, *9*, 26518−26530.
(63) Hasa, I.; Passerini, S.; Hassoun, J. Toward High Energy Density Cathode Materials for Sodium-ion Batteries: Investigating the Beneficial Effect of Aluminum doping on the P2-type structure. *J. Mater. Chem. A* **2017**, *5*, 4467−4477.
(64) Thangavel, R.; Samuthira Pandian, A.; Ramasamy, H. V.; Lee, Y.-S. Rapidly synthesiszed, Few layered Pseudocapacitive SnS2 Anode for High Power Sodium ion Batteries. *ACS Appl. Mater. Interfaces* **2017**, *9*, 40187−40196.
(65) Campillo-Robles, J. M.; Artetxe, X.; del Teso Sánchez, K.; Gutiérrez, C.; Macicior, H.; Röser, S.; Wagner, R.; Winter, M. General Hybrid Asymmetric Capacitor Model: Validation with a Commercial Lithium ion Capacitor. *J. Power Sources* **2019**, *425*, 110−120.
(66) Vignesh, R. H.; Sankar, K. V.; Amaresh, S.; Lee, Y. S.; Selvan, R. K. Sensors and Actuators B: Chemical Synthesis and characterization of $MnFe_2O_4$ nanoparticles for Impedometric Ammonia gas sensor. *Sens. Actuators, B* **2015**, *220*, 50−58.
(67) Hu, M.; Hu, T.; Li, Z.; Yang, Y.; Cheng, R.; Yang, J.; Cui, C.; Wang, X. Surface Functional Groups and Interlayer Water Determine the Electrochemical Capacitance of $Ti_3C_2T_x$ MXene. *ACS Nano* **2018**, *12*, 3578−3586.
(68) Luo, J.; Fang, C.; Jin, C.; Yuan, H.; Sheng, O.; Fang, R.; Zhang, W.; Huang, H.; Gan, Y.; Xia, Y.; Liang, C.; Zhang, J.; Li, W.; Tao, X. Tunable Pseudocapacitance Storage of MXene by Cation Pillaring for High Performance Sodium-ion Capacitors. *J. Mater. Chem. A* **2018**, *6*, 7794−7806.

https://dx.doi.org/10.1021/acsami.9b19288
ACS Appl. Mater. Interfaces 2020, 12, 10268−10279

(69) Ding, J.; Hu, W.; Paek, E.; Mitlin, D. Review of Hybrid Ion Capacitors: From Aqueous to Lithium to Sodium. *Chem. Rev.* **2018**, *118*, 6457−6498.
(70) Ding, J.; Wang, H.; Li, Z.; Cui, K.; Karpuzov, D.; Tan, X.; Kohandehghan, A.; Mitlin, D. Peanut Shell Hybrid Sodium ion Capacitor with Extreme Energy-Power Rivals Lithium ion Capacitors. *Energy Environ. Sci.* **2015**, *8*, 941−955.

https://dx.doi.org/10.1021/acsami.9b19288
ACS Appl. Mater. Interfaces 2020, 12, 10268−10279